

# Direct numerical simulation of the two-dimensional speed bump flow at increasing Reynolds numbers



Mikhail L. Shur<sup>a</sup>, Philippe R. Spalart<sup>b</sup>, Mikhail Kh. Strelets<sup>a,\*</sup>, Andrey K. Travin<sup>a</sup>

<sup>a</sup> Peter the Great Saint-Petersburg Polytechnic University, 195257 Saint-Petersburg, Russia

<sup>b</sup> Boeing Commercial Airplanes (Boeing Senior Technical Fellow, retired), USA

## ARTICLE INFO

### Keywords:

Smooth surface separation  
Speed Bump configuration  
DNS  
RANS  
Effect of Reynolds number

## ABSTRACT

The Speed Bump flow model was designed by Boeing to provide a mildly three-dimensional flow with separation from a very smooth surface, strongly controlled by the turbulence. Experiments are conducted by several teams, as are simulations, over a range of Reynolds numbers. Direct Numerical Simulations (DNS) are not possible for the full 3D geometry of width  $L$ , leading several groups to conduct DNS over a two-dimensional geometry, in other words the cross-section of the full geometry, with periodic lateral conditions and a typical domain width of  $0.04L$ . This does not allow precise comparisons with experiment, but code-to-code comparison is instructive. A shallow separation bubble is present, as intended. The domain width becomes marginal after reattachment, where the boundary layer is much thicker. The Reynolds number based on  $L$  has been  $10^6$ , so far in the literature, which causes partial relaminarization and tends to defeat the purpose of testing turbulence models. Flow visualisation is clear on this. Here, we present results at the Reynolds number  $10^6$  and  $1.4 \times 10^6$ , and the higher value essentially eliminates relaminarization. Detailed results are shown, including studies of domain width, grid resolution, and numerical dissipation. The turbulence models give inaccurate results for skin friction, already in the intense favourable pressure gradient, which causes the formation of an internal boundary layer; the separation prediction on the other hand is reasonable. The wall curvature seems to play a role. The present results also provide trustworthy data to test Large-Eddy Simulation (LES), especially if using a Wall Model (WMLES). The comparisons will have a preliminary character until the results of the ongoing detailed experiments and of DNS at even higher Reynolds number and with a wider domain are available and carefully compared.

## 1. Introduction

**Smooth-body separation** is rightly considered to exhibit a major weakness in our understanding of turbulence, and in our ability to accurately calculate flows of high industrial value. This was already recognized in the 1980's, and no breakthroughs have taken place since then. The numerical capabilities of CFD now bring us close to convergence even for rather complex geometries such as an airliner wing in high-lift configuration, so that the physical errors in turbulence modelling will dominate relatively soon; our estimate is for it to happen within the 2020's, thanks to the increase in computer power and to automatic grid adaptation. This leads the community to vigorous efforts designing new turbulence experiments. Benefits are expected from modern measurement techniques such as Oil-Film Interferometry and Particle-Image Velocimetry, but equally important is the much-improved teaming arrangement between modellers, CFD experts, and

experimentalists. Separated flows are so sensitive that very accurate boundary conditions are required; also, ignoring the effects of the wind-tunnel side-walls on a 2D geometry is unacceptable.

The Speed Bump (SB) configuration (Fig. 1), designed by Boeing and first presented by Slotnick (2019), is recent and has good potential to provide a flow with mild separation fully controlled by the turbulence over an absolutely smooth geometry, and essentially no influence of the side-wall boundary layers. The setting is that the bump is placed on a splitter plate, which is centered in a wind tunnel, itself having a square cross-section of size  $L$ , which is the reference length throughout. The geometry is specified by the following formula

$$y(x, z) = h \frac{1 + \operatorname{erf}\left(\frac{L/2 - 2z_0 - |z|}{z_0}\right)}{2} \exp\left[-\left(\frac{x}{x_0}\right)^2\right] \quad (1)$$

in which  $x$  is the streamwise,  $y$  the vertical, and  $z$  the lateral

\* Corresponding author.

E-mail address: [strelets@mail.rcom.ru](mailto:strelets@mail.rcom.ru) (M.Kh. Strelets).

directions. The origin is at the center of the bump, so that the  $z$  interval is  $[-L/2, L/2]$ . Three parameters define the bump shape, namely a height,  $h$ , and two widths,  $x_0$  and  $z_0$ . Two other parameters needed to specify the flow are the height of the ceiling,  $H$ , and the thickness of the incoming boundary layer, which may be controlled locally or through the length of the upstream splitter plate. The sixth parameter is the Reynolds number, based on  $L$ .

Internal CFD work has shown a definite sensitivity to turbulence model, and experimental work of Williams et al. (2020) a similar sensitivity to Reynolds numbers. The experimental trend is the opposite of “simple” Reynolds-number effects, and quite suggestive of partial laminarization; this will be confirmed by DNS. A favourable aspect of this problem, for rigorous comparisons, is that it is fully defined by one formula and six numbers.

Recent similar experimental efforts include RETTINA in Germany (Knopp et al., 2015), Simmons et al. (2019) at Notre Dame in the US, and the VPI bump in the US (Lowe et al., 2020), while the NASA Hump (Greenblatt et al., 2006) is older but in much use. All these use the wind-tunnel wall boundary layer, which is thicker than that over the SB, which uses a splitter plate both to reduce the thickness and to make it independent of the wind-tunnel characteristics. A large NATO Applied-Vehicle Technology programme, AVT-349, federates eleven experiments for boundary layers out of equilibrium, covering smooth and rough walls and pressure gradients, in 2D and 3D (see <https://www sto nato int/Lists/test1/activitydetails.aspx?ID=16794>). The NASA smooth-step effort initiated by Disotell and Rumsey (2017), as well as the Sandia transonic bump (Lynch et al., 2020) involve axisymmetric bodies and are free of side-wall effects; the averaged solution is expected to be two-dimensional, which is a definite advantage both for modelling and for future DNS and similar efforts, which in principle can be conducted in a sector of well under  $360^\circ$ , as, e.g., in the DNS of Spalart et al. (2017) of the experiment of Bachalo and Johnson (1986). Note, however, that in unpublished work both our group and Sandia have obtained RANS solutions which are far from being axisymmetric and strongly depend on the particular RANS model used, so that great caution is in order. The Reynolds numbers are somewhat limited, intentionally in the Sandia case, to facilitate DNS. Most of these efforts include variations of the Reynolds number and/or the intensity of the pressure gradient, both of which can be revealing. Each of these experimental flow models has strengths and weaknesses, and together with the SB will provide new knowledge the modelling community will attempt to use wisely without of course disregarding older work. All the flow models have been designed in close collaboration between modellers, experimentalists and CFD experts, which is now the norm (and also applies to the NASA Juncture Flow (Rumsey, 2018)); added to the new instrumentation capabilities, this gives hope for a significant body of new knowledge. The modelling effort may use a blend of classical thinking and Machine Learning, depending on how fast ML matures. This applies both to pure RANS and to Wall-Modelled LES.

DNS studies of separation bubbles include those of Coleman et al. (2018) and Abe (2017). Unlike the SB, these have straight walls (allowing in one case a spectral numerical method) and enter the

Adverse Pressure Gradient (APG) region without first having a Favourable Pressure Gradient (FPG), which is an advantage. They made possible a wider range of Reynolds number than has been achieved on the SB so far, without relaminarization. Both specify a suction/blowing distribution on an upper boundary, with irrotational flow. Unfortunately, an experimental duplication of this boundary condition does not appear possible in contrast with the SB. The knowledge of turbulence coming from these studies complements that from the SB.

The simulation by Bentaleb et al. (2012) is labelled LES, but very close to DNS. It has a simple smooth downward-facing step and combines smooth-body separation with a thick separated layer akin to that from a sharp backward-facing step. This simulation is also “free-standing,” without experimental confirmation.

The published experimental literature on the SB is by Williams et al. (2020). The Reynolds number  $Re_L$  based on the model width,  $L$ , ranged from  $1.2 \times 10^6$  to  $3.6 \times 10^6$ . The measurements were primarily wall pressure and wall streamlines. The Boundary Layer (BL) was tripped reliably at  $x/L = -1$  ( $x = 0$  corresponds to the SB crest – see Fig. 1); the control over the incoming BL is a key aspect of all studies of this flow. The pressure distributions show less separation at the lower Reynolds numbers, which would be surprising in a fully turbulent flow because the BL, having the same origin near the trip, would be thicker. A plausible explanation is some relaminarization which depresses the skin friction at low  $Re_L$ , thus over-riding the thickening effect that exists upstream. There is a clear tendency for the pressure distributions to become Re-independent in the upper range. RANS results, which cannot capture relaminarization, indeed showed the opposite trend to the experiments.

SB studies use as a reference length scale the width  $L$  of the model, even though it is physically irrelevant in 2D. The streamwise extent of the visible bump is roughly  $[-0.35L, 0.35L]$  as seen in Fig. 1. The range for  $Re_L$  in research wind tunnels is roughly from  $10^6$  to  $4 \times 10^6$ . DNS literature as of 2020 contains simulations with  $Re_L = 10^6$ , periodic lateral conditions over a 2D reduction of the geometry, and a typical domain width  $L_z$  equal to  $0.04L$ ; this includes Uzun and Malik (2020) and Balin et al. (2020). Their two solvers and ours are fully independent, which is valuable in terms of estimating the remaining uncertainty in DNS; it is larger in this kind of non-trivial flow than in simpler cases such as the Taylor-Green Vortex or channel flow. Here, we briefly compare our results with those of Uzun and Malik (2020) and Balin et al. (2020); the differences are moderate, but the initial expectation that DNS from different teams would be in near-perfect agreement was denied.

The value  $L_z = 0.04L$  was agreed upon between the present authors and the authors of the two mentioned DNS studies of SB flow to make code-to-code comparisons rigorous (as mentioned, in the 2D geometry,  $L$  loses any physical meaning, but the periodic domain width is meaningful, unless it is quite large, for instance  $0.5L$ ). This domain size is adequate up to the separation line since the BL thickness is about  $0.015L$ , but not after reattachment, as will be shown below using two-point correlations: values such as  $0.1L$  are desirable in the future if the reattachment region is a focus of attention.

The simulations at  $Re_L = 10^6$  very much confirmed the partial

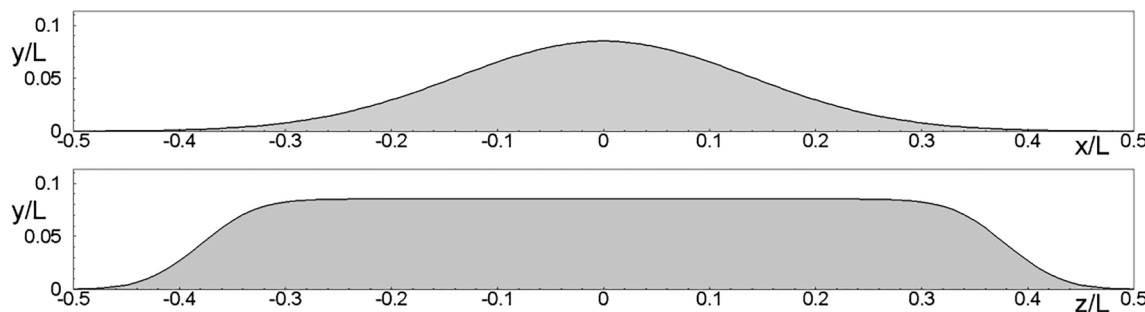


**Fig. 1.** 3D Speed Bump configuration. Upper: side view; lower: end view (symmetry plane at  $z/L = 0$ , side-wall at  $z/L = \pm 0.5$ , ceiling at  $y/L = 0.5$ ).

relaminarization, and the serious difficulties encountered by RANS turbulence models. Maybe surprisingly, the difficulties begin long before separation, in the intense FPG which prevails on the front side of the bump. Such regions are often considered “easy,” but it could be because in external-flow practice their boundary layers are too thin to influence the flow globally. The skin-friction coefficient is taken as the primary measure of success for the RANS models and shows much larger deviations from the DNS than the pressure coefficient does.

The relaminarization encountered at  $Re_L = 10^6$  constitutes a strong motivation to reach higher values, because it gives the RANS models an “excuse” for failing. So, although this phenomenon is observed in some practical applications, given the RANS state of the art and the high Reynolds numbers typical of the most important aerodynamic flows, limiting the challenge to fully turbulent cases is wise. Our computing power limited us to  $1.4 \times 10^6$ , with only a slightly larger domain width  $L_z/L = 0.05$ ; this  $Re_L$  increase eliminates almost all the relaminarization tendency, but not the DNS-RANS disagreement in the FPG. Thus, the 2D SB flow at  $Re_L = 1.4 \times 10^6$  presents a highly challenging test case for RANS, probably mingling the effects of pressure gradient and wall curvature, while the  $Re_L = 10^6$  flow may serve as a special test case for development and validation of the RANS models claiming to accurately predict laminarization. The paper also presents grid-resolution and numerical-dissipation variations. We proceed from here with a description of the numerical method, the sensitivity studies, and then the results with an emphasis on code-to-code comparisons, followed by conclusions.

## 2. Flow problem and numerical approach

The exact formulation of the 2D problem considered in the present DNS is illustrated in Fig. 2, which also serves to reveal the shape of the SB, which is given by  $y(x) = h\exp[-(x/x_0)^2]$ , where  $h/L = 0.085$ ,  $x_0/L = 0.195$ ,  $y_c/L = 0.5$  ( $y_c$  is the coordinate of the channel ceiling).

In the streamwise direction, the computational domain extends from  $x/L = -1.33$  to  $1.0$ . It includes a region  $-1.33 \leq x/L \leq -1.0$  with uniform velocity at the inflow and a slip lower wall (or symmetry condition) and a region  $-1.0 \leq x/L \leq 1.0$  with a non-slip wall. This approach was pioneered by NASA Langley Research Center (2021) (Turbulence Modeling Resource, <https://turbmodels.larc.nasa.gov/bump.html>) and solves a problem which would occur if a uniform velocity were imposed at  $x/L = -1.0$  (the BL origin), namely the creation of spurious vorticity opposite to that inside the BL at the edge of the turbulent layer. At  $-1.0 \leq x/L \leq -0.6$ , the flow is treated with RANS and further downstream DNS is employed. The BL is considered turbulent starting from its origin. In the present simulation this is reached by giving turbulence model inflow values that ensure an immediate transition to turbulence. At  $x/L = -0.6$  (the DNS inlet) a Synthetic Turbulence Generator (STG) of Shur et al. (2014) is placed, which injects 3D time-dependent fluctuations of the velocity to initiate the DNS.

The RANS region used the SA model in its recent low-Reynolds-number version (Spalart and Garbaruk, 2020), which raises the momentum thickness by about 10% relative to the original SA model (Spalart and Allmaras, 1992). The momentum-thickness Reynolds number  $Re_\theta$  at the STG, with  $Re_x = 0.4 \times 10^6$ , is about 1080. The reality is that various experiments and simulations do not agree exactly on the

incoming BL thickness, especially after the DNS recovers from the imperfections of the STG, but the differences have been successfully narrowed. Note that the thinning of the BL in the FPG, from about  $x/L = -0.2$  to  $0$ , visible in Fig. 2, weakens its memory when approaching the region of most interest.

The ceiling of the wind tunnel is replaced by a displaced boundary on which a slip condition applies. The BL on that wall is of little interest. Its displacement thickness was obtained from a RANS simulation of the full domain with a viscous upper wall and is shown in Fig. 3 along with the analytical fit which was used. Only the slope of this curve really matters.

The computations are carried out with the use of the in-house NTS code (Shur et al., 2004). This is a structured cell-centered finite-volume high-order CFD code accepting multi-block overset grids of Chimera type and capable of the simulation of turbulence in the framework of a full range of turbulence-resolving approaches. The DNS capability of the code has been demonstrated, e.g., by Spalart, Strelets and Travin (2006), Spalart et al. (2015), and Spalart et al. (2017). The incompressible branch of the code employed in the present simulations uses the flux-difference splitting method of Rogers and Kwak (1988). The inviscid fluxes are approximated with the use of a 4th order central scheme and for the viscous fluxes the 2nd order central scheme is applied. Finally, the time integration is performed with the use of implicit 2nd order backward Euler scheme with sub-iterations.

The two grids used in the simulations are defined in Table 1 and the finer one, Grid 1, is displayed in Fig. 4.

It has  $5809 \times 255 \times 301$  nodes in the  $x$ ,  $y$ , and  $z$  directions, respectively ( $445.9 \times 10^6$  nodes total). Grid 2 is coarser by a factor of 2 in the wall-parallel directions (it has  $2905 \times 183 \times 151$  nodes or  $80.3 \times 10^6$  nodes total). The wall-unit spacings given in Table 1 are defined by the friction velocity at the DNS inlet  $x/L = -0.6$ ; at  $x/L = 0$ , the friction velocity is higher by a factor of about 1.3, so that the normalized spacings are typical of DNS practice, for instance about 8 in the lateral direction  $z$ .

The time step in the simulations on Grid 1 and Grid 2 is equal to  $0.5 \times 10^{-4} L/U_0$  and  $10^{-4} L/U_0$ , respectively (this ensures the CFL number less than 1.0 in a major part of the domain). All the simulations are performed for about 4 convective time units  $L/U_0$  (2.5 pass-through times), 2 of which were needed for getting statistically mature solutions and 2 for accumulating the turbulent statistics.

## 3. Results

### 3.1. Overview

Ideally, experimental or numerical results are presented with a range of uncertainty that is both rigorous and not so loose it is unhelpful. Unfortunately, the DNS community has been unable to achieve this. The reasons include the very large number of degrees of freedom and time steps, the nonlinearity of the equations, the fact that a convincing numerical refinement increases the computing cost by over an order of magnitude combined with the great desire to set a high enough Reynolds number, and in many cases the approximate nature of the inflow or initial conditions. In some literature, DNS is called “exact,” and this is simply not correct. Here, we address this issue both with tests internal to our study, and limited comparisons with DNS by two independent teams

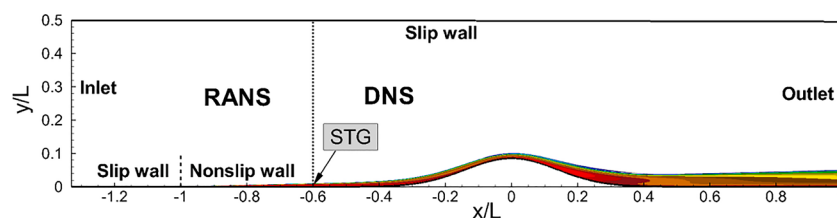


**Fig. 2.** Computational domain in XY-plane used for DNS. Color: vorticity magnitude field from low-Re SA RANS at  $Re_L = 10^6$ .

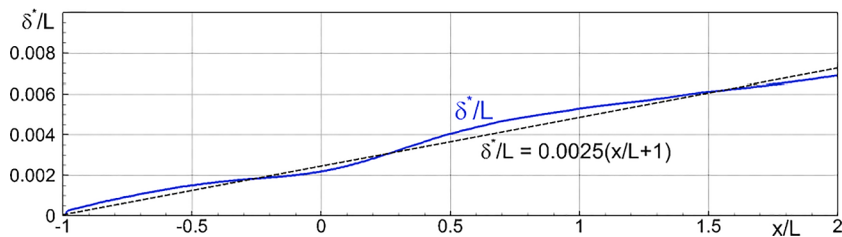


**Fig. 3.** Streamwise distribution of the displacement thickness predicted by RANS.

**Table 1**  
Major parameters of Grids 1 and 2 at DNS inlet.

Grid	$\Delta_x/L = 2 \times$	$\Delta_{y,1}/L =$	$\Delta_{y,max}/L = 1.33 \times$	$\Delta_z/L = 1.33 \times$
1	$10^{-4}$	$10^{-5}$	$10^{-4}$	$10^{-4}$
	$\Delta_x^+ = 9$	$(\Delta_{y,1}^+) =$	$(\Delta_{y,max}^+) = 6$	$\Delta_z^+ = 6$
		0.45		
Grid	$\Delta_x/L = 4 \times$	$\Delta_{y,1}/L =$	$\Delta_{y,max}/L = 2.67 \times$	$\Delta_z/L = 2.67 \times$
2	$10^{-4}$	$10^{-5}$	$10^{-4}$	$10^{-4}$
	$\Delta_x^+ = 18$	$\Delta_{y,1}^+ = 0.45$	$\Delta_{y,max}^+ = 12$	$\Delta_z^+ = 12$

(Uzun and Malik (2020) and Balin et al. (2020)). Differences between sources give a lower bound for the uncertainty, but certainly not an upper bound, considering that all solvers could err in the same direction. In particular, they all allow a non-zero numerically-induced loss of turbulent kinetic energy.

The problem of turbulent channel flow comes close to having “full” agreement between different teams, many of which make their data available. It is free of initial and inflow conditions. Of course, the numerical solutions are not exact, and the time samples are finite. In addition, the periodic domain size is only moderately large (and would be insufficient for Couette flow), and recent interest in very long “superstructures” in the core region has put pressure on it. Therefore, even this problem has not been “fully solved” yet.

The Taylor-Green Vortex is free of any arbitrary domain size or initial conditions. It is deterministic, but truly turbulent. Very close agreement between the best solutions has been observed, including for sensitive measures such as the peak dissipation rate and at sufficient Reynolds numbers. On the other hand, it does not test wall boundary conditions, curvilinear coordinates, or non-uniform grids; these are important

sources of error in flow such as the SB, the principal ones being grid resolution, numerical dissipation in the algorithm, lateral domain size, and inflow conditions. In the next section they are explored using plausible measures, but again a rigorous upper bound on the error is not available. A practical definition of a sufficiently small uncertainty could be that the uncertainty estimate is much smaller than the disagreement between the DNS and the tool that is being informed by the DNS, be it a theory or a RANS model.

The rest of this Section is organized as follows. We first present results of the internal quality tests and compare our results with those of other SB DNS studies at  $Re_L = 10^6$  (§§ 3.2 and 3.3, respectively) and then present and discuss the principal results of the simulations at the two Reynolds numbers (§ 3.4). Finally, § 3.5 is devoted to an evaluation of RANS models’ capability to predict the SB flow.

### 3.2. Internal quality tests

We begin with grid resolution. Recall that Grid 1 is the finer one, and Grid 2 can be described as somewhat coarse. This depends on the region, and in particular on the value of the friction velocity  $u_\tau$ .

Figs. 5 and 6 present visualizations of vorticity. The effect of the coarser resolution is evident in the  $x$ - $y$  plane, in the outer part of the boundary layer. It is less obvious in the wall flow pattern; the structures in Grid 2 are still fine there. On the other hand, the local minimum in skin friction near  $x/L = 0.02$  is higher for Grid 2. While this could be due to variations in time, Fig. 7 for the time-average  $C_f$  confirms that this minimum is sensitive to resolution more than any other region; this could reflect the subtle kinetic-energy losses mentioned above. Note also that Grid 2 gives a higher  $C_f$ , both in the fully turbulent and the lamination regions. In contrast to this, the average pressure coefficient  $C_p$

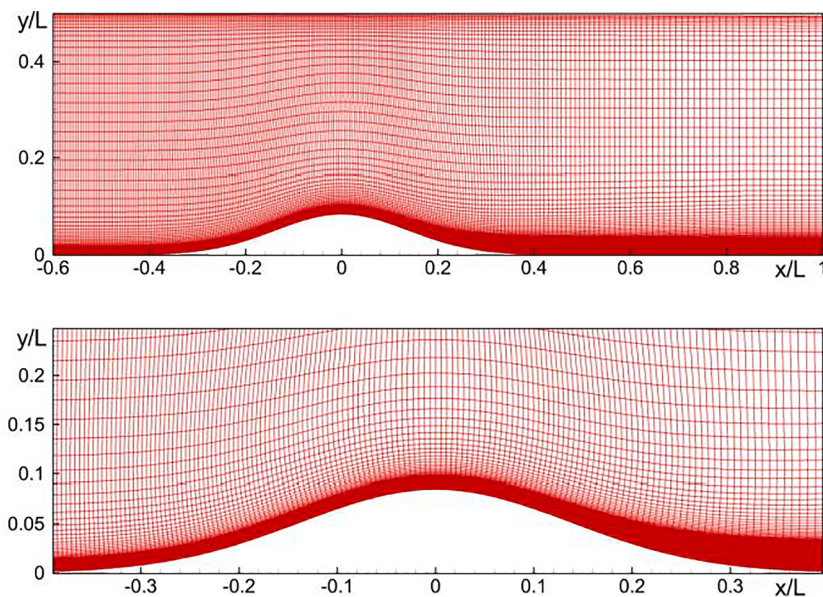


**Fig. 4.** Grid 1 in XY-plane and its zoomed in fragment (only every 24th line in x-direction and every 3rd line in y-direction are shown).

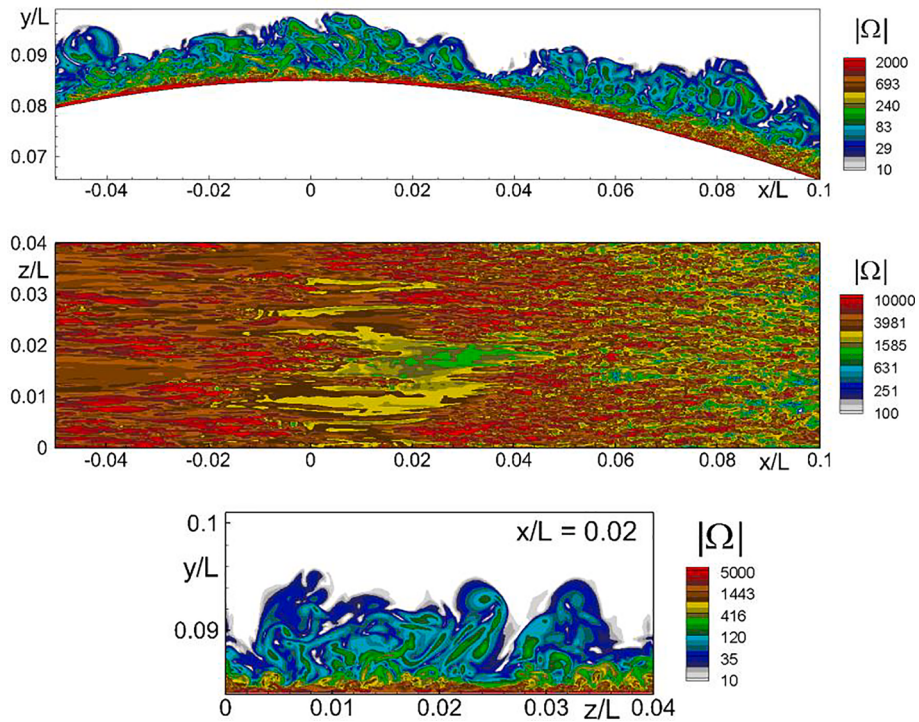


**Fig. 5.** Upper and middle frames: snapshots of vorticity magnitude in an XY-plane and at the bump surface near the SB crest. Lower frame: snapshot of vorticity magnitude in ZY plane at  $x/L = 0.02$ . DNS on Grid 1, domain width  $L_z/L = 0.04$ .

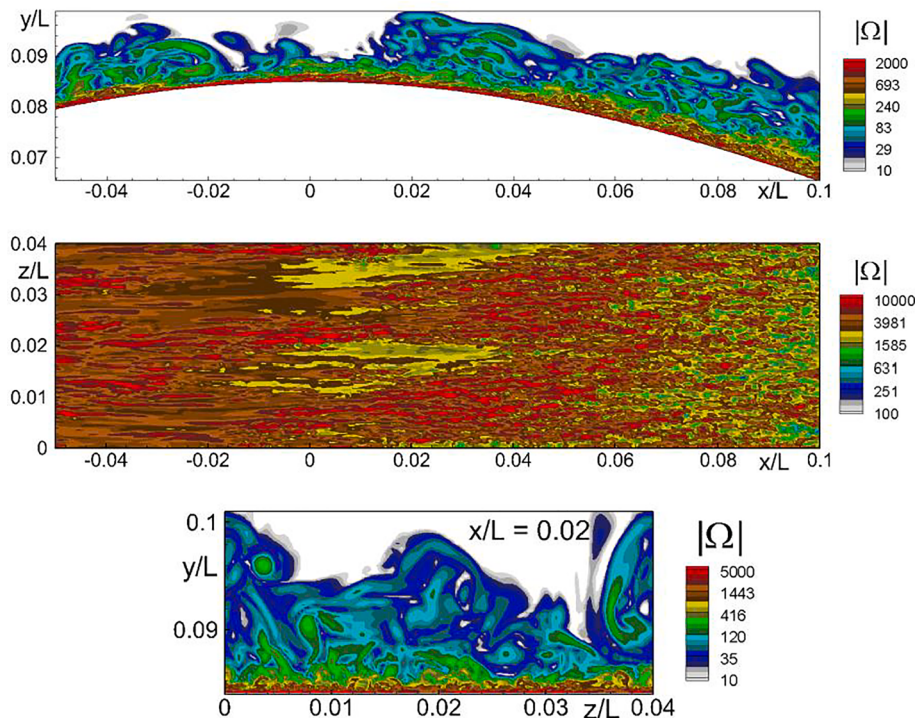


**Fig. 6.** Same, as in Fig. 5, from DNS on Grid 2.

also shown in Fig. 7 is almost insensitive to grid-refinement, which is explained by the thin boundary layer and the shallow separation zone.

Another semi-quantitative message from Figs. 5 and 6 is that based on the small wall flow structures the lateral period equal to  $0.04L$  in the region of the flow with low local skin friction is quite sufficient. On the other hand, a searching examination of the figures could suggest that the

alternating high and low skin-friction bands occur with two of each in both simulations, which would not be a coincidence, but we do not know of a stability theory (possibly involving streamwise vortices) for these phenomena. The views in a ZY plane in Figs. 5 and 6 do not suggest a pattern with two “structures” within  $L_z$ . The BL thickness is seen to be around  $0.013L$ , and therefore close to the width of the low-friction

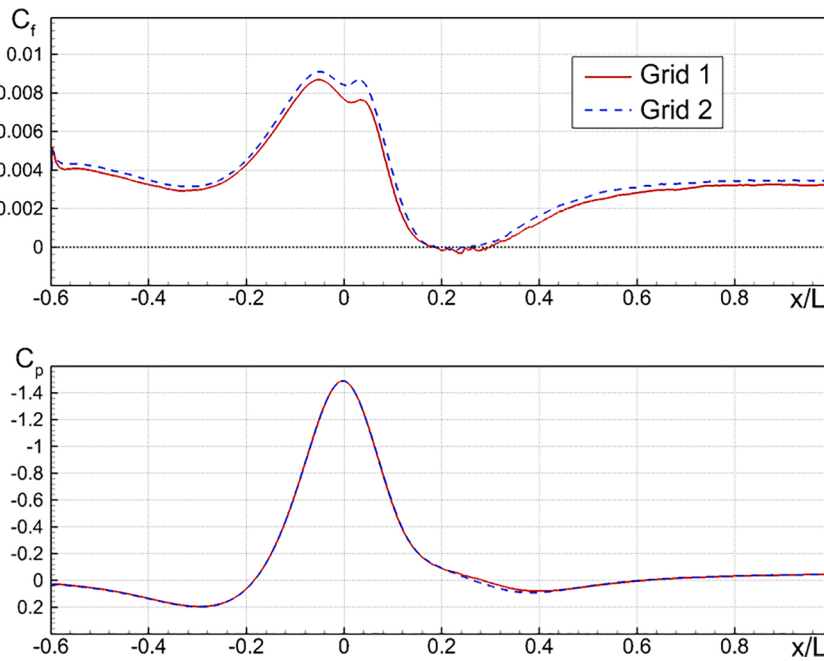


**Fig. 7.** Effect of grid on the streamwise distributions of skin friction (upper frame) and pressure (lower frame) coefficients.

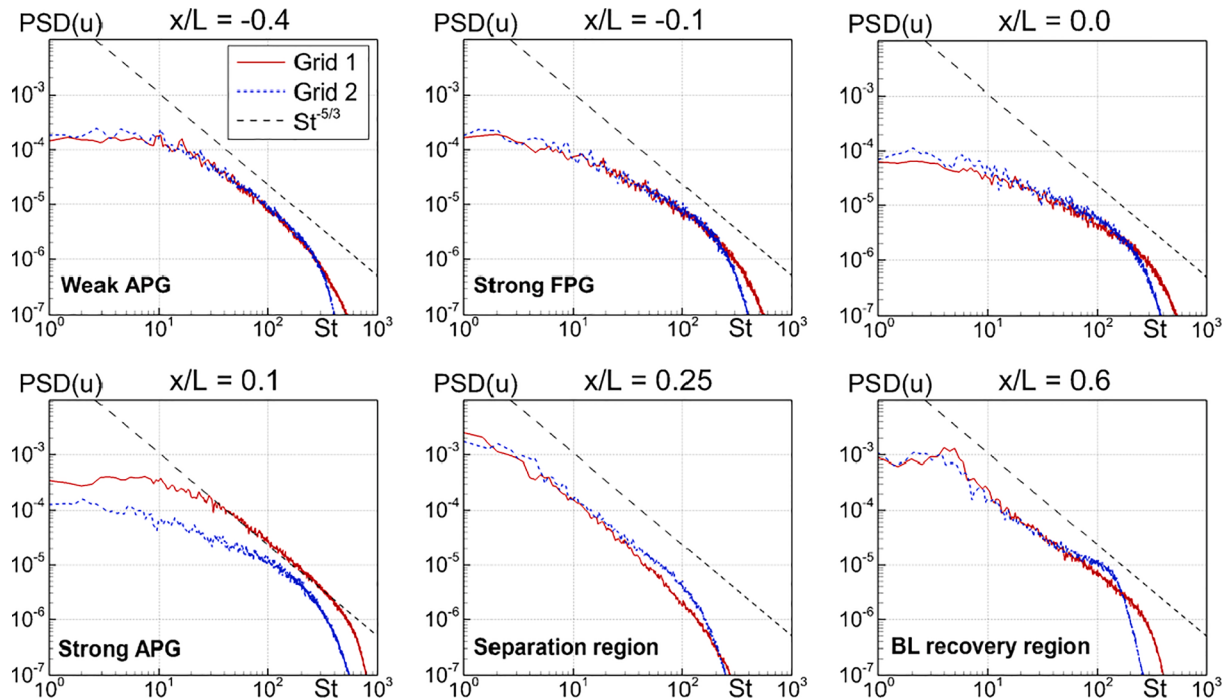
patches. In other words, the patches are not large in  $\delta$  units. The thickness can also be compared with the radius of curvature,  $R_c$ , namely  $0.22L$ : the ratio  $\delta/R_c$  of about 0.06 is in fact large enough for curvature effects to be significant. We base this statement on the guideline of Bradshaw (Bradshaw, 1973), namely that curvature effects on turbulence are an order of magnitude larger than would be predicted from simple estimates.

Fig. 8 displays temporal spectra at various  $x$  locations, and a height of  $0.004L$  above the wall; this is about  $1/3$  of the BL thickness. The spectra from the two grids differ enough to indicate that the numerical truncation is significant in the Kolmogorov viscous range. They are different from end to end at  $x/L = 0.1$ , shortly after the region with the most skin-

friction difference; the effect exists across the BL. In the separation and recovery regions, the thickness Reynolds number has become sufficient for an inertial range to be present. Curiously, at  $x/L = 0.6$ , the slope over more than a decade of frequencies is about  $-1.43$ , instead of  $-5/3$ . This might be a sign of vigorous high-frequency turbulence stimulated by the rising skin friction.

In Fig. 9, the resolution effects on the peaks of turbulent kinetic energy and Reynolds shear stress (in wall axes) are far from simple. The two grids agree closely in the approach region, and then not as well, with difference switching sign repeatedly.

Overall, the resolution studies indicate that the durable grid, namely Grid 1, is adequate while not achieving full “grid convergence” by any



**Fig. 8.** Effect of grid on the Power Spectral Density of the streamwise velocity fluctuations.

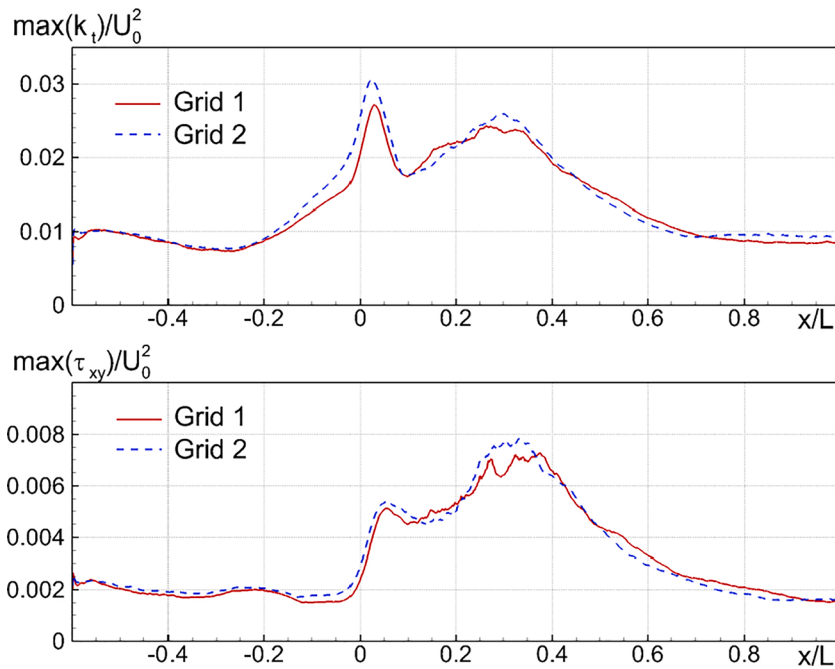


**Fig. 9.** Effect of grid on the streamwise distributions of the maximum turbulent kinetic energy (upper frame) and shear stress (lower frame).

means.

We now turn to the effect of another decision with much effect on the computing cost, namely the domain width  $L_z$ . We only have comparisons between the standard value of  $0.04L$  and the smaller  $0.02L$ . Near the bump crest, Fig. 10 tends to support the idea that a natural period for the low-friction patches is near  $0.02L$ . Note that this phenomenon will essentially disappear at the higher Reynolds number. In the separation and reattachment region, especially beyond  $x/L = 0.25$ , the

visualization clearly indicates that  $0.02L$  is insufficient.

This is confirmed by Fig. 11, through two-point correlations. The  $u-u$  correlations with  $L_z/L = 0.02$  are completely unacceptable beyond  $x/L = 0.25$ . Many of the other curves are acceptable, allowing of course for statistical noise.

Fig. 12 confirms the severe effect of the narrow domain on the thicker parts of the BL, while indicating that the effect is weak for  $x/L < 0.3$ . This strongly suggests that  $L_z = 0.04L$  is more than adequate

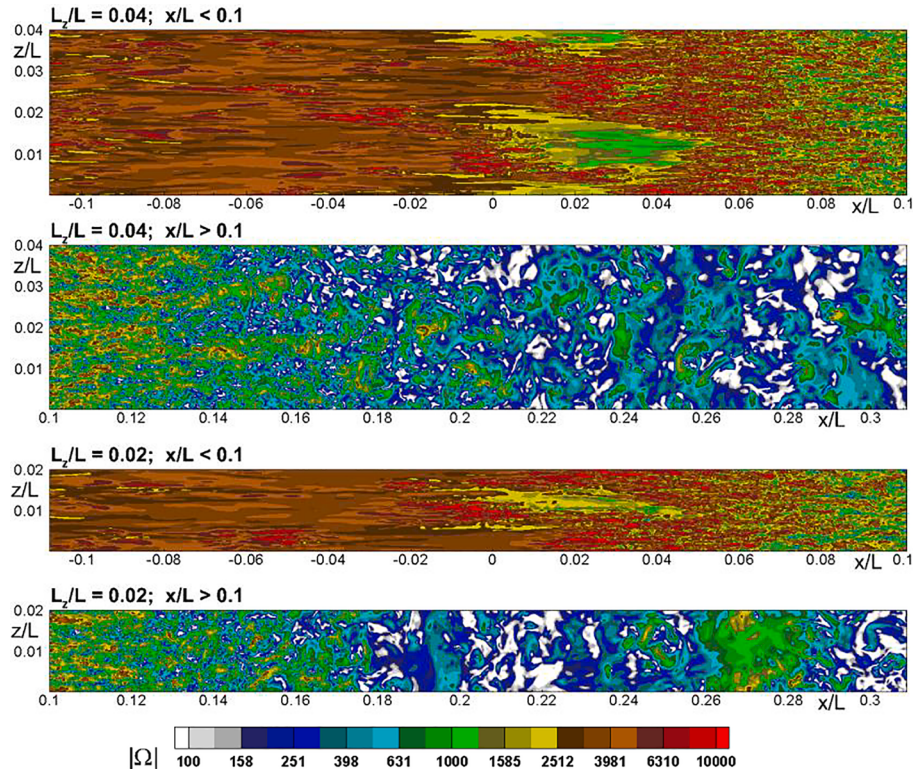


**Fig. 10.** Effect of domain width on snapshots of vorticity magnitude at the bump surface. First and second frames:  $L_z/L = 0.04$ ; third and fourth frames:  $L_z/L = 0.02$ .

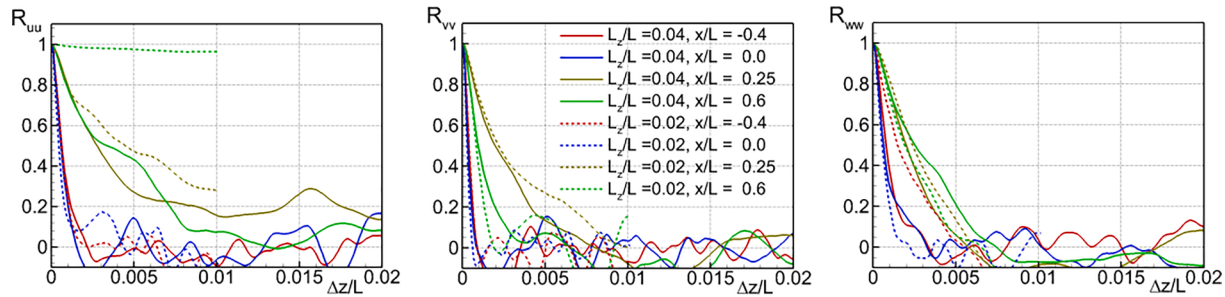


**Fig. 11.** Effect of domain width on two-point spanwise correlations of the velocity components at  $d_w/L = 10^{-3}$ . Solid lines:  $L_z = 0.04L$ ; dashed lines:  $L_z = 0.02L$ .

in the entry, FPG, and separation regions.

Finally, Fig. 13 illustrates the effect of explicit numerical dissipation introduced by the use of the weighted approximation of the inviscid fluxes in the momentum equations,  $F_{inv} = (1 - \sigma)F_{CD} + \sigma F_{UPW}$ , where  $\sigma$  is the weight parameter,  $F_{CD}$  corresponds to the 4th order centered approximation of these fluxes used in all the simulations discussed above, and  $F_{UPW}$  corresponds to their 5th order upwind biased approximation. In particular it compares results of the “baseline” simulation ( $\sigma=0$ ) and two additional simulations performed, one with  $\sigma = 0.03$  and the other with  $\sigma = 0.06$ . In terms of the added numerical dissipation, the first value may be considered as relatively low and the second one as tangible. The figure shows that the effect is quite strong, especially in the laminar and separation regions. This test was conducted in the narrow domain, in order to contain the computing cost, but this limits the region of full validity of the findings to the region  $x/L < \approx 0.1$ . It is very plausible that the differences residing in the  $[-0.1, +0.1]$  range are the cause of the differences over  $[0.1, 0.6]$ , the mechanism being that a lower skin friction reduces the BL thickness and therefore the extent of separation. The correspondence between skin friction and pressure is as expected, namely, deeper flow reversal is associated with a clearer plateau on the pressure. Also note the negligible effect for  $x/L < -0.12$ , although the friction velocity is high, calling for finer resolution. Again, the region of partial relaminarization truly exaggerates the numerical factors.

### 3.3. Comparison with other DNS studies

We begin with velocity profiles in the entry region, which is less challenging but conditions the rest of the flow. It is also crucially dependent on the STG. The left frame of Fig. 14 shows excellent agreement of our DNS with the standard flat-plate flow (ZPG BL) and logarithmic layer at  $x/L = -0.5$ , even though the distance from the STG is only  $0.1L$ , and the BL thickness slightly above  $0.01L$ . In other words, the recovery is complete in less than  $10\delta$ . This will be confirmed in Fig. 16. The right frame of Fig. 14 again reveals an excellent log law, and minor differences relative to the results of Uzun and Malik (2020). At this station, the BL has entered a mild Adverse Pressure Gradient (APG) caused by the concave curvature at the beginning of the bump (this curvature is reflected in the slope of the profile outside the BL).

We follow with visualizations, covering the entry/FPG region and partial relaminarization in Fig. 15. The qualitative agreement between the two studies is remarkable, with the streaks becoming longer and wider, then much lower levels, followed by a rapid return of fine-scale streaks around  $x/L = 0.05$ .

The direct skin-friction comparison in Fig. 16 is less favorable. The steps near  $x/L = 0.05$  in our simulations and those of Uzun and Malik (2020) and Balin et al. (2020) are quite different. This echoes the differences seen in the internal quality checks above, including in Fig. 13. In contrast, the FPG region and the extent of separation are fairly close, despite the fact that Uzun and Malik (2020) used the recycling approach (Uzun and Malik, 2018) rather than the STG, with the recycling section

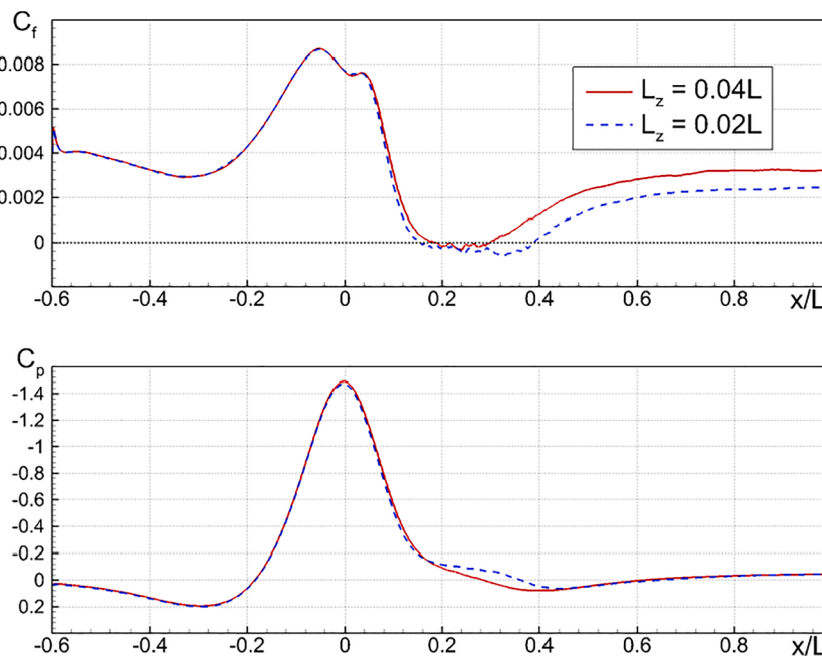


**Fig. 12.** Effect of domain width on the streamwise distributions of skin friction (upper frame) and pressure (lower frame) coefficients.

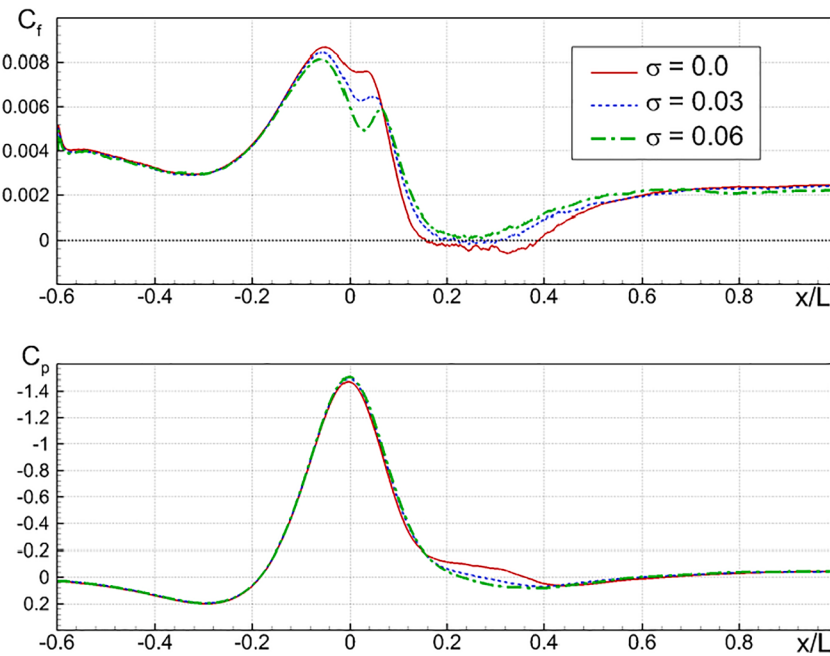


**Fig. 13.** Effect of  $\sigma$  on the streamwise distributions of skin friction (upper frame) and pressure (lower frame) coefficients. Grid 1,  $L_z = 0.02$ .

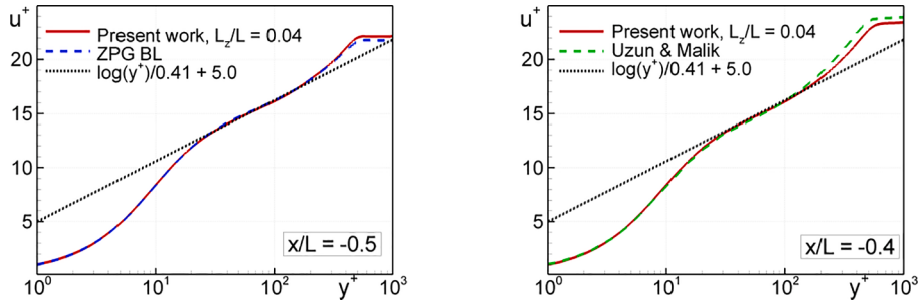


**Fig. 14.** Mean velocity profiles at  $x/L = -0.5$  in SB flow and in the ZPG BL (left) and in a mild APG region of the SB flow (right). Both in law of the wall coordinates.

at  $x/L = -0.8$ . Finally, all the three studies agree very well in the FPG region, which is very far from a standard BL. Nonetheless, the  $C_f$  levels from our simulation are higher than from theirs, both in the entry region and the final recovery region; these should have been the most predictable. The differences are as high as 5%, which is more than was expected from careful DNS studies in 2020. We checked the BL thicknesses, and the difference was much too small to explain the  $C_f$  difference. This may be compared with DNS in channel flow. The published datasets, kindly collected for us by Dr. H. Abe of JAXA, reveal differences of about 1.5%; this is a much smaller scatter, but channel flow has been studied since the 1980's and unlike the SB flow does not require curvilinear coordinates, or a turbulence generator.

It should be noted in this context that as seen in the lower frame of Fig. 16, in fact, the effect of the parameter  $\sigma$  is not negligible in fine code-to-code comparisons. Particularly, in the entry region the more dissipative runs with our code move towards Uzun & Malik's and Balin *et al.*, although only part-way, and in the most challenging laminar-reflective region, their results are between ours with  $\sigma = 0$  and 0.06. We can hope that, over the next year or two, the definitive DNS result will be established in the entry region, and even in all the fully turbulent regions. A scatter of 1 to 2% is desirable.

### 3.4. Principal results at the two Reynolds numbers

We have arrived at the simulation of the  $Re_L = 1.4 \times 10^6$  flow which

is the core motivation of the work. The domain width was marginally increased, from  $0.04L$  to  $0.05L$ , for the new run. The grid in the simulation has the same structure as the fine (Grid 1) used for the simulation at  $Re_L = 10^6$ , but grid-steps in the streamwise and spanwise directions and the maximum step in the wall-normal direction as well as the time-integration step are additionally reduced by a factor of 1.4. As a result, the grid now has  $\sim 0.95 \times 10^9$  points.

We again begin with visualizations in Fig. 17, which strongly suggest that  $Re_L = 1.4 \times 10^6$  is sufficient to eliminate the partial relaminarization to a large extent. The streaks are still wider and longer around  $x/L = -0.06$ ; since the friction velocity is high there, their dimensions in wall units are definitely larger: a visual estimate of the streak spacing is  $0.0025L$ , and  $C_f \approx 0.009$ , giving 235 in wall units (the standard value is 100). Notice the tighter pattern returning for  $x/L > 0$ . Still, there are no large patches with low friction. This situation will provide a clearer target for RANS studies in particular. The length scales of the turbulence are smaller, as expected with an increase by a factor of 1.4.

A visual impression of Fig. 17 suggests that the domain width is more than sufficient in this region. In order to more rigorously assess the domain width over the entire simulation domain, Fig. 18 presents two-point correlations at various  $x$  stations. They are very adequate for  $x/L < 0$ , become marginal at 0.25, and are clearly inadequate at 0.6. This is what leads us to an estimate of at least 0.1 for the domain width of a fully-valid simulation.

Fig. 19 illustrates the separation and reattachment. The separation is

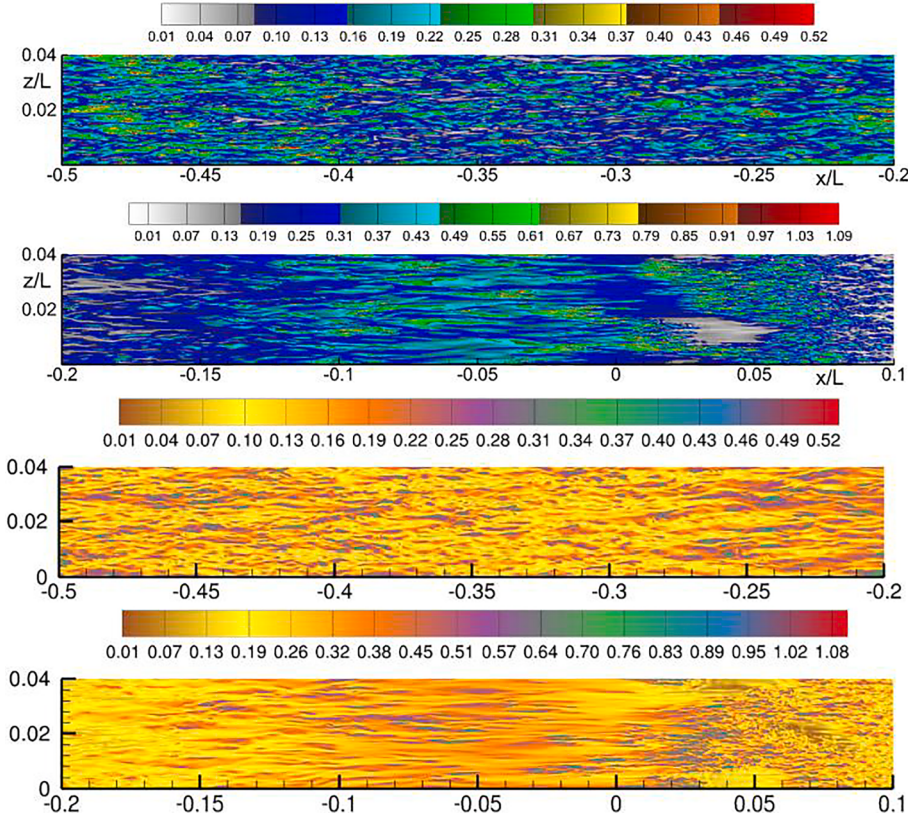


**Fig. 15.** Snapshots of streamwise velocity component at a near-wall grid surface, along which  $4 < y^+ < 6$  from the present DNS (first and second frames) and from that of Uzun & Malik, 2020 (third and fourth frames).

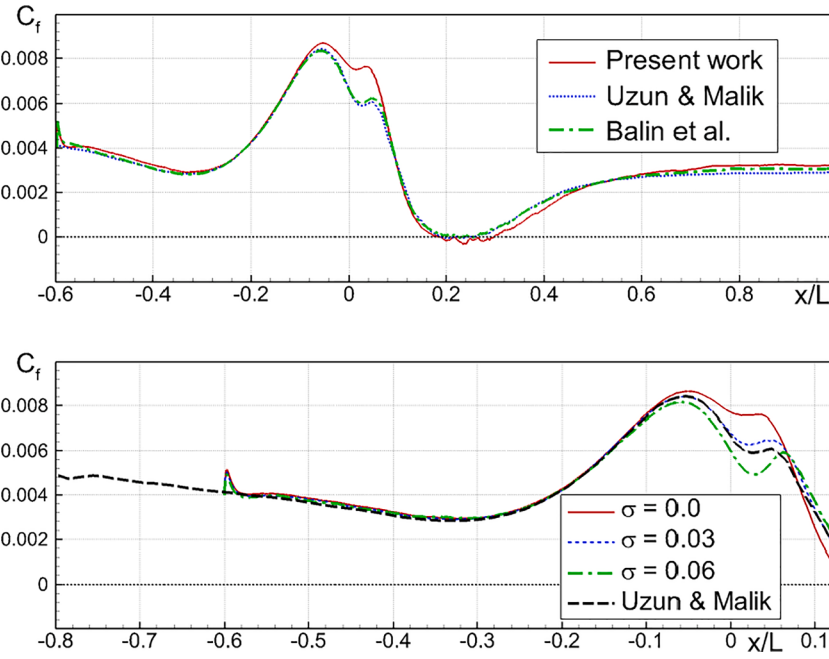


**Fig. 16.** Streamwise distributions of skin-friction coefficient predicted by present DNS and DNS of Uzun and Malik, 2020 and of Balin et al., 2020 (upper frame) and zoomed-in fragment of the upper frame with additional results of present DNS at different values of  $\sigma$ .

thicker at the higher Reynolds number, which is the opposite of the classical effect, and is consistent with experimental finding by Williams et al. (2020), focused on pressure distributions. We attribute it to the higher skin friction, which will be shown shortly. It cannot be argued simply from the figures that the BL thickness  $\delta$  is increased, but the loss

of momentum near the wall can well cause the earlier separation.

Fig. 20 illustrates the complex differences between the low- and high-Reynolds number flows. Beginning with skin friction,  $C_f$  is slightly lower at higher  $Re_L$ , both in the entry region up to  $x/L = -0.1$  and in the recovery region; this is typical in simple boundary layers. Near the crest,

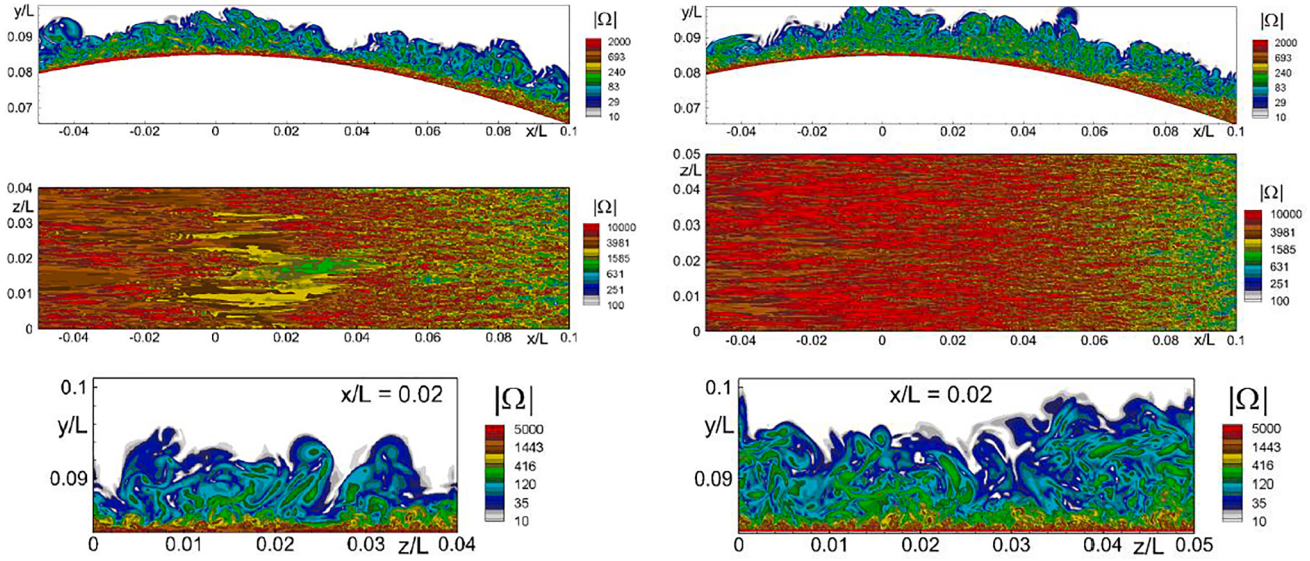


**Fig. 17.** Effect of Reynolds number on instantaneous fields of vorticity magnitude. Upper row: XY-plane. Middle row: SB surface. Lower row: ZY plane  $x/L = 0.02$ . Left column:  $Re_L = 10^6$ ; right column:  $Re_L = 1.4 \times 10^6$ .

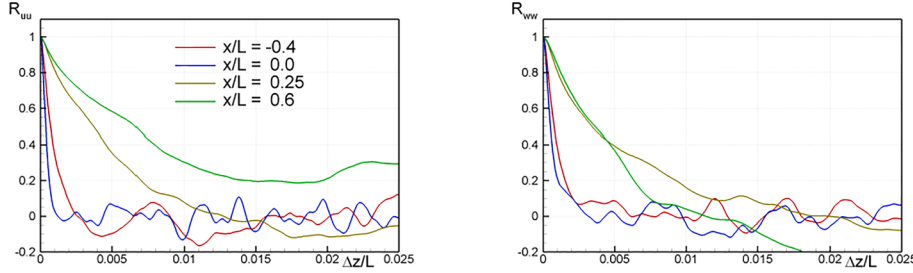


**Fig. 18.** Two-point correlation coefficients near the SB surface at different streamwise locations at  $Re_L = 1.4 \times 10^6$ .

at  $x/L = 0$ , the higher Reynolds number case does not have the drop, followed by a rise and a second drop. The rise at the higher  $Re_L$  does weaken visibly around  $x/L = -0.06$ , which is consistent with our qualitative comments on Fig. 17. This region could be described as “still turbulent, but with a slight weakness.” This slight weakness is too small to seriously invalidate comparisons with RANS models, shown below. In the region from  $x/L = 0.1$  to  $0.4$ , the flow reversal is much wider, as noticed in the visualizations. This is reflected by a much more definite plateau on the pressure distributions shown in the lower frame of Fig. 20, again in good qualitative agreement with the experiment of Williams et al. (2020). As also seen in the figure, the direction of change in pressure distribution is consistent with the Williams et al. finding of “more separation at higher Reynolds number”. This represents a “reverse Reynolds-number effect”. The SSG-LRR model fails to predict this trend; other models, not shown, also fail. They all predict the conventional trend in which a thinner boundary layer reduces the tendency for separation. This indicates that the 2D version of the bump considered in the DNS is quite representative of the center region of the 3D bump, as intended in its design.

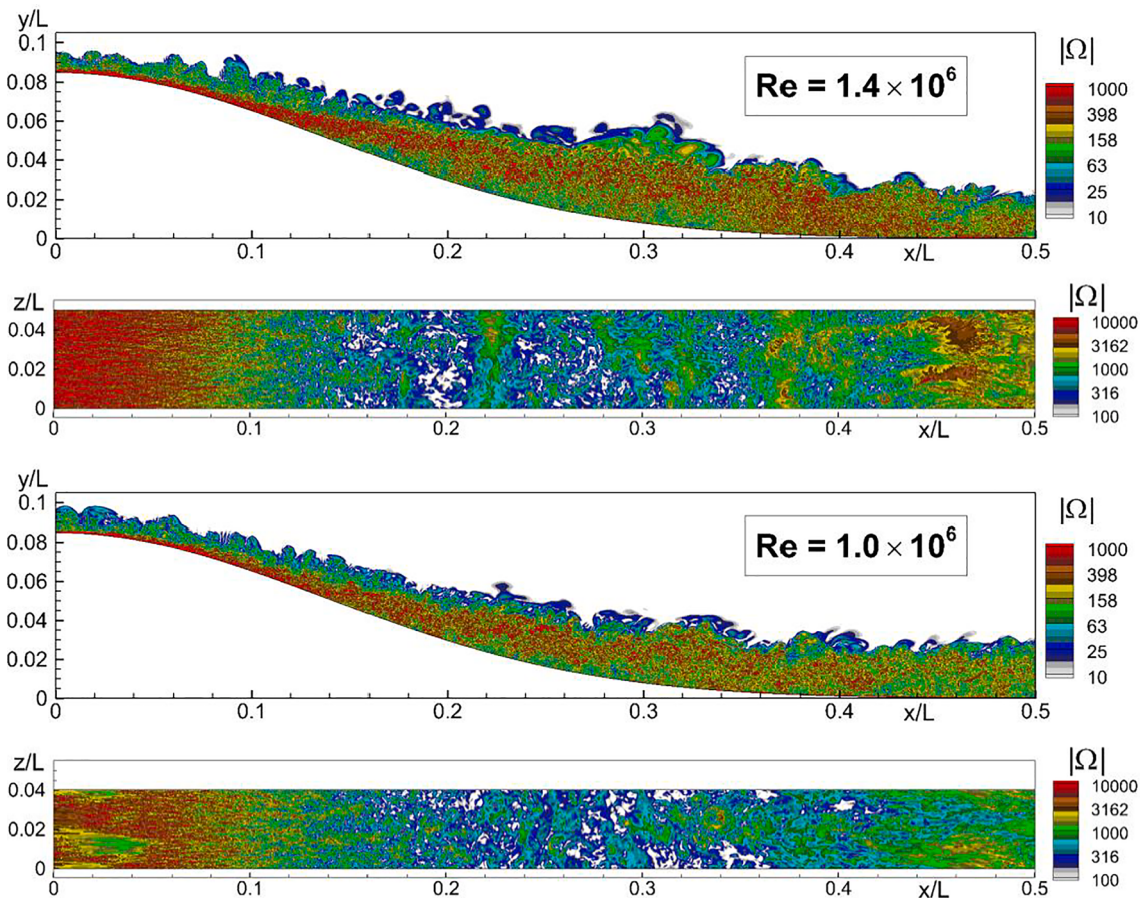
Fig. 21 confirms Fig. 19, now in the time- and z-averaged field. Both the reversed-flow region and the shear layer above it are noticeably thicker.

Fig. 22 displays the BL thicknesses. The integrals are based on the vorticity-based pseudo-velocity of Spalart and Watmuff (1993), and  $\delta$  is defined by the pseudo-velocity having reached 99% of its final value. Up to  $x/L \approx -0.05$ , the boundary layer is slightly thinner at the higher  $Re_L$ , as expected since they have the same origin. Then, the trend reverses, particularly for the displacement thickness, due to the higher skin

friction at higher  $Re_L$  seen in Fig. 20. We believe this is a direct cause for flow reversal occurring near  $x/L = 0.12$ , rather than 0.19, and also for the much wider region with reversal. We also observe the same trend in the experimental data for pressure.

Fig. 23 reveals wide differences in the turbulent kinetic energy, as well as the complex physics in the FPG. The distributions at  $x/L = -0.5$  are almost identical and typical of those with zero pressure gradient, having a plateau near 0.003 with a near-wall peak. At  $x/L = -0.1$ , the BL thickness inherited from the entry region is almost  $0.015L$ , but a much thinner and stronger inner layer has developed under about  $y/L = 0.001$ , clearly distinct from the smoother outer turbulence, which has decayed (convex curvature may have played a role in that). This will represent a major difficulty for Large-Eddy Simulation and probably RANS modeling as well. At  $x/L = 0.0$ , the higher Reynolds number gives a higher peak, consistent with the higher  $C_f$ . At  $x/L = 0.1$ , the peaks have already migrated away from the wall, to about  $y/L = 0.0025$ ; the convected outer-layer turbulence is still easily identified, and slowly decaying. At  $x/L = 0.2$  and  $0.4$ , the separation is higher at the higher  $Re_L$ , and the energy is higher due to being less confined by the wall. At  $x/L = 0.6$ , the recovery patterns are similar, although the high- $Re_L$  case still has 2/3 more energy. Ultimately, the TKE again peaks very near the wall, as its production rises in the high-shear layer; however, the recovery process is far from complete at 0.9, which will also challenge the models.

Fig. 24 expands on the complexity of the turbulent behavior at both Reynolds numbers. In particular, while at  $Re_L = 10^6$  the sudden slope changes near  $x/L = -0.04$  and near 0.06 can be associated with unusual behavior in the skin friction, at  $Re_L = 1.4 \times 10^6$  there is a steep decrease



**Fig. 19.** Effect of Reynolds number on instantaneous fields of vorticity magnitude in XY-plane (first and third frames) and at the SB surface (second and fourth frames) for  $0 \leq x/L \leq 0.5$ .

between 0 and about 0.08, followed by a steep rise in the separated region, where the skin friction is essentially zero. The skin friction and the peak TKE and shear stress do not parallel each other: the high- $Re_L$  case has lower skin friction, but stronger turbulence. This trend lingers in the recovery region, beyond  $x/L = 0.6$  all the way to the outflow boundary at  $x/L = 1.0$ .

### 3.5. Evaluation of RANS models

A strong motivation for SB and similar efforts is to inform the assessment and when possible the improvement of RANS models. As mentioned, relaminarization is extremely challenging, and an orderly research plan is to seek fully turbulent cases first. Here, we view the skin friction as the most revealing quantity, and directly test versions of the Spalart-Allmaras model (Spalart and Allmaras, 1992; Spalart and Shur, 1997; Spalart and Garbaruk, 2020), the  $k-\omega$  SST model (Menter, 1994), and the SSG-LRR  $\omega$  Reynolds Stress Transport (RST) model (Eisfeld et al., 2016a; Eisfeld et al., 2016b). Fig. 25 is at the lower Reynolds number and Fig. 26 at the higher one.

We begin with the trends in the entry and recovery regions. In both cases, the RANS results are grouped together, and lower than the DNS results, except for the RST model after reattachment. In the entry region, in principle the least challenging one, the models agree better with Uzun and Malik's results. The agreement in the partial-relaminarization region is very poor, but that was expected, and the distance is smaller at  $Re_L = 1.4 \times 10^6$ .

More serious is the disagreement in the FPG region, roughly  $x/L = [-0.15, 0]$ . It is worst with the SA models, but still definite with SST and RST. The disagreement is smaller at the higher Reynolds number, but DNS today is far from powerful enough to anticipate the behavior at

industrial Reynolds numbers. This conflicts with the widespread thought that adverse pressure gradients and separation are the dominant issue with RANS models. It also strongly suggests that the behaviour of the models in APG can be isolated in the present flow; this behaviour, and the location of separation, result from an extended "history" of the boundary layer. At  $Re_L = 1.4 \times 10^6$ , the separation point and the peak negative  $C_f$  predicted by RANS are quite accurate, but it would not be prudent to view that as a conclusive success. For instance, some SA versions show excellent agreement in the reversed region at  $Re_L = 10^6$ , but following major disagreement over  $x/L = [-0.18, 0.08]$ , which makes the agreement probably fortuitous.

An unusual finding at  $Re_L = 1.4 \times 10^6$  is that RANS predicts reattachment earlier than DNS, in contrast with similar flows such as the NASA Hump (Greenblatt et al., 2006). Unfortunately, conflicting demands from different flows are frequent when attempting to improve models.

Besides key outputs such as skin friction, DNS can be used to guide model development locally, and we give an example here. From a DNS, an "effective eddy viscosity" can be calculated as the scalar that gives the best fit to the Reynolds-stress tensor (see Spalart et al., 2017). This information has been used for "human intelligence" work and is beginning to be used for Artificial Intelligence work. We solved the PDE of the RANS models in the velocity field of the DNS, rather than running a normal CFD solution; the advantage of this procedure is that it reduces the "history effects" on the mean flow field (such as a much thinner or thicker BL), therefore giving a more local, although still PDE-governed, behaviour for the model. Tests with a coupled mean-flow/model solution give similar findings.

The pattern in the upper frame of Fig. 27 is striking, in that the DNS

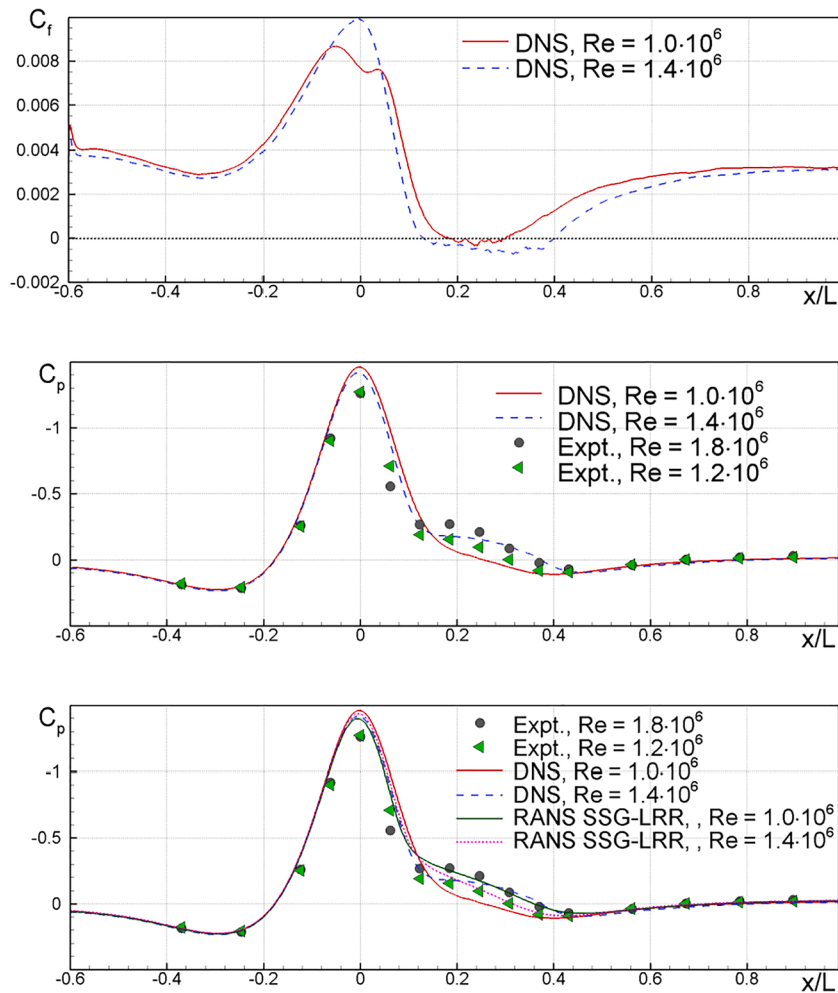


**Fig. 20.** Effect of Reynolds number on streamwise distributions of skin-friction (upper frame) and pressure (middle and lower frames) coefficients. Symbols: experiment of Williams et al., 2020.

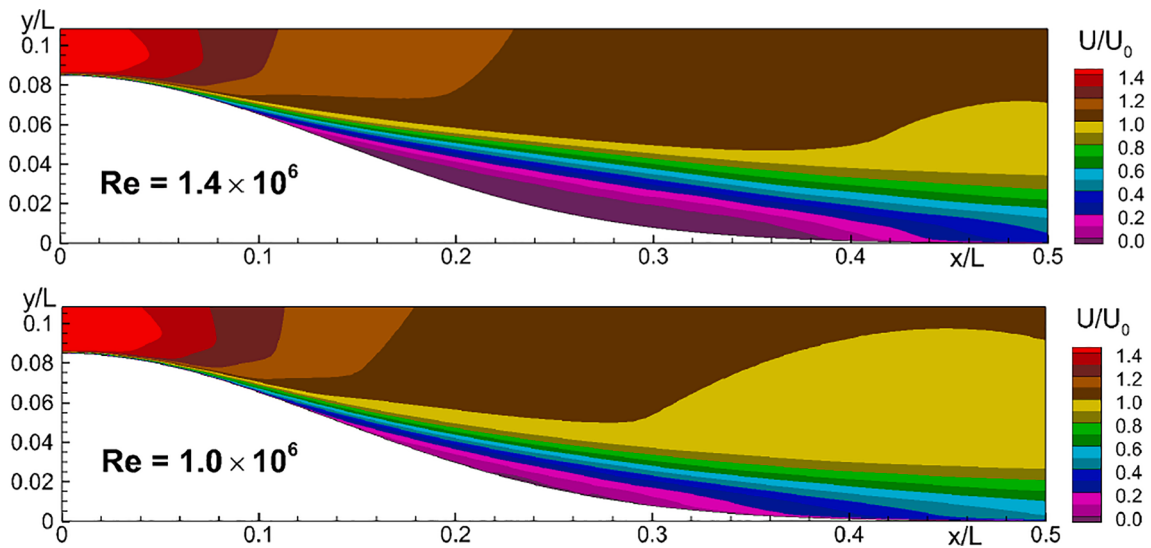


**Fig. 21.** Effect of Reynolds number on mean streamwise velocity field in XY-plane.

eddy viscosity after showing close agreement with RANS (the middle frame) essentially vanishes at the crest of the bump. This is far out of reach of a Partial Differential Equation that “transports” eddy viscosity,

as confirmed by the SA results in which no such collapse is seen. What complicates the interpretation is that this phenomenon could well be attributed to convex streamline curvature. This is known to weaken

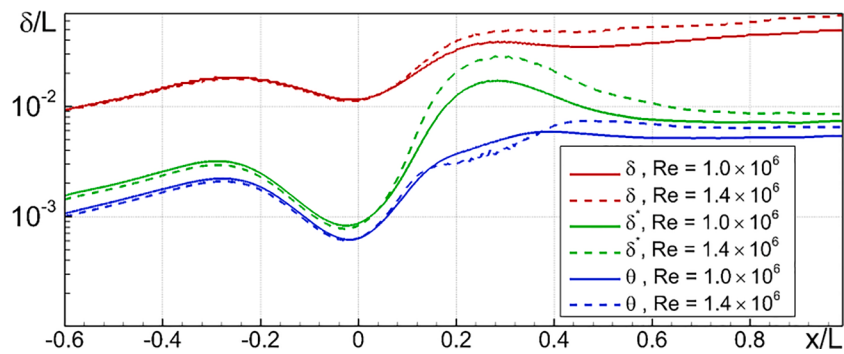


Fig. 22. Effect of Reynolds number on streamwise distribution of BL thicknesses.

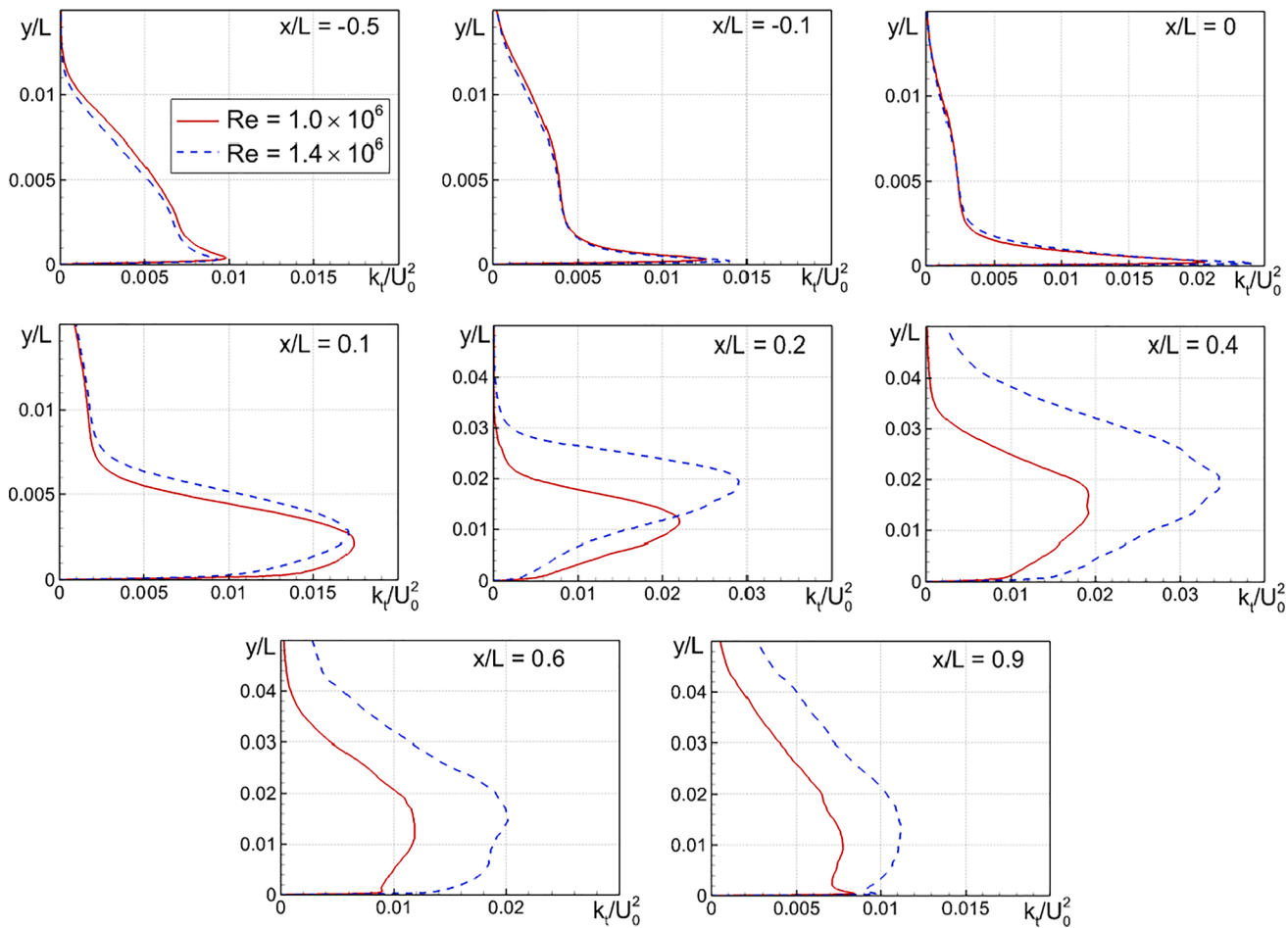


Fig. 23. Effect of Reynolds number on profiles of turbulent kinetic energy.

turbulence, especially in terms of the alignment between the strain tensor and the stress tensor, which is powerful in the least-squares procedure; a valid interpretation of the least-squares eddy viscosity is that it is the scalar that would provide the correct rate of TKE production. In other words, the eddy viscosity field deduced from the DNS exhibits a region of zero or even negative TKE production, which is unusual but has been seen in other separated flows. Not shown is the fact that in this region, vorticity naturally is transported as usual, whereas the strain rate collapses like the DNS eddy viscosity does. This is all far out of reach of eddy-viscosity models, although the effect in the momentum equation is small, due to the short region in which this is happening. We attribute this more to curvature than to pressure gradient, without any rigorous proof. Note that the Rotation-Curvature

correction to the SA model made little difference; this is not a rigorous criterion either. A striking result is that from the Reynolds-Stress Model (the lower frame in Fig. 27): the eddy viscosity “extracted” from the stresses collapses much like it does in the DNS, indicating that the curvature effect is captured (on the other hand, Fig. 25 showed that the FPG effect is not captured well).

#### 4. Conclusions and future work

The two-dimensional reduction of the Speed Bump flow was studied by Direct Numerical Simulation at a Reynolds number of  $10^6$ , which had been reached in the literature, and at the new value of  $1.4 \times 10^6$ . This increase was not fully successful in eliminating all tendencies to

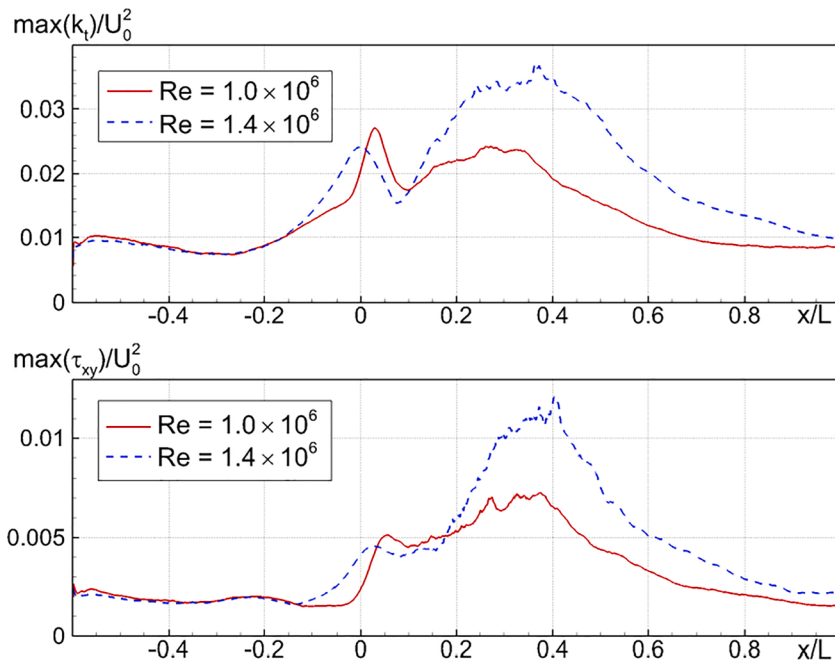


**Fig. 24.** Effect of Reynolds number on streamwise distributions of maximum turbulent kinetic energy (upper frame) and of maximum shear stress (lower frame).

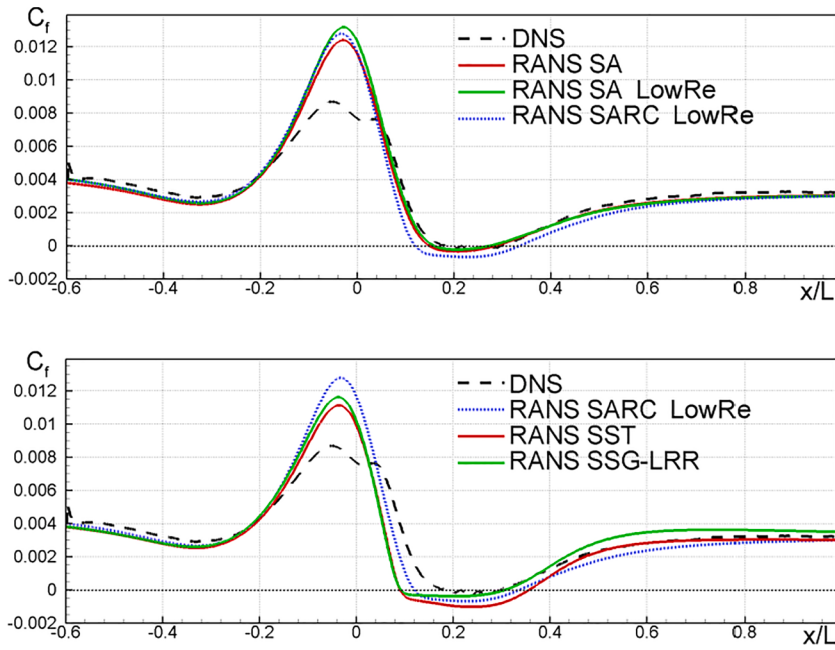


**Fig. 25.** Comparison of streamwise distributions of skin-friction predicted by different RANS models and by DNS at  $Re_L = 10^6$ .

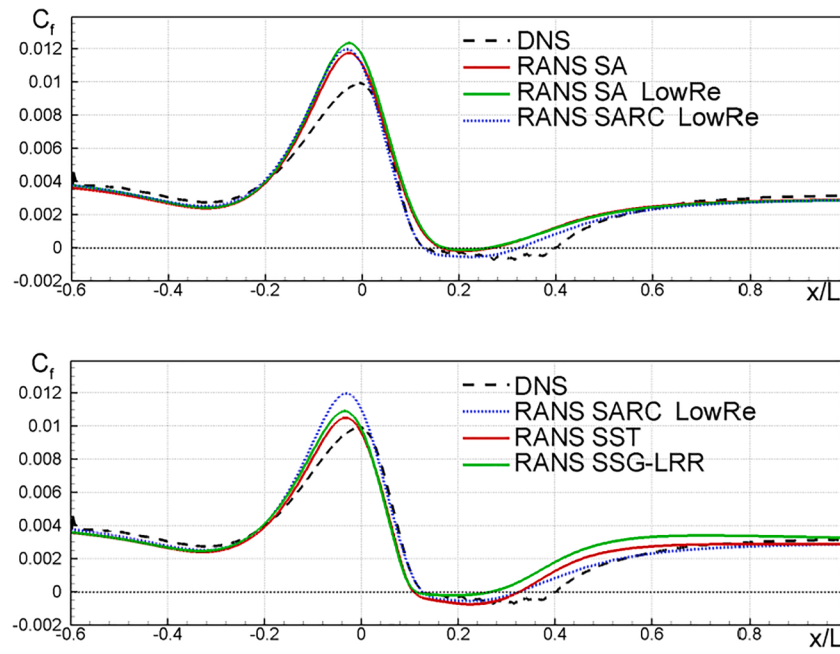
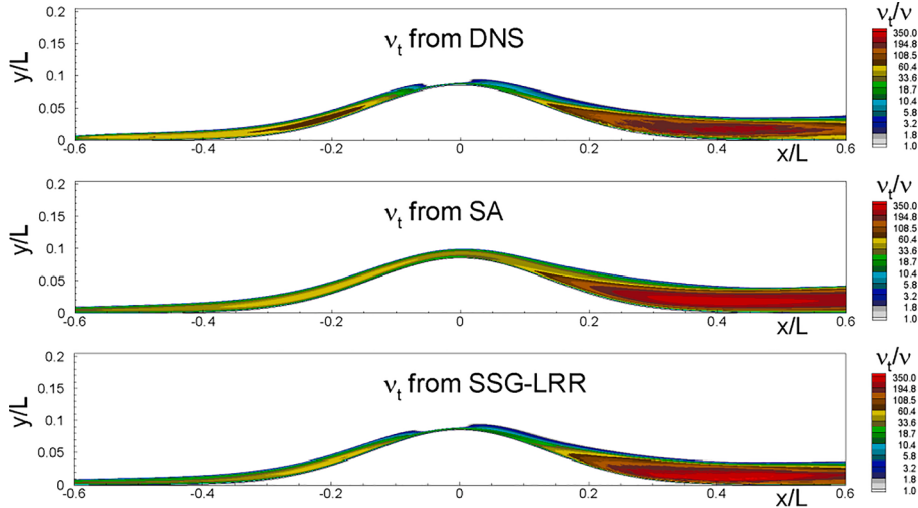
weakening of the turbulence, but nearly so. Note that the weakening can be partly blamed on convex wall curvature, which is stronger than expected, but the 40% increase in Reynolds number was dominant. The flow has a very rich behaviour in this Reynolds-number range, including a reverse Reynolds-number effect on the extent of separation. This largely confirms the experimental findings of Williams et al. (2020). The flow also develops challenging internal layers and long-lived non-standard features including in the protracted recovery region.

The comparison with DNS works by other teams exhibited differences somewhat larger than expected, of the order of 5% for the skin friction in the relatively simple (and fully turbulent) entry region. The differences were magnified in the region of partial relaminarization observed at  $Re_L = 10^6$ , which may be less surprising. The effects of grid

resolution and numerical dissipation were also quite large in that region, which fortunately disappears at higher Reynolds numbers.

RANS models were generally expected to become inaccurate near separation, but all of them distinctly fail even at the higher Reynolds number in the favourable pressure gradient, which admittedly is very strong although not sustained enough to cause a complete relaminarization. All models give an excess of skin friction in the FPG. The two-equation and Reynolds-Stress Transport models are more accurate than the one-equation model, even with its curvature correction. This failure in FPG makes the understanding of the APG and separation regions proper quite difficult.

The future studies of obvious value entail a considerable increase in computing cost. Runs at  $Re_L = 2 \times 10^6$  definitely should ensure fully

Fig. 26. Same as in Fig. 25 at  $Re_L = 1.4 \times 10^6$ .Fig. 27. Comparison of eddy-viscosity fields extracted from the DNS solution (upper frame) and from the SA transport and the RSM equations fed by the mean velocity field from DNS (middle and lower frames) at  $Re_L = 10^6$ .

turbulent behaviour throughout, giving an unquestionable target for RANS models. A wider periodic domain, raising  $L_z/L$  from 0.04 to at least 0.1, is necessary for quantitative accuracy in the region of thick recovering boundary layer, since  $\delta/L \approx 0.06$  there. Thus, a factor of at least 10 in computing cost relative to  $1.4 \cdot 10^6$  with the present domain width is in order. As of the beginning of 2021, we know through personal communications of three teams that are planning runs at  $Re_L = 2 \times 10^6$ . In our opinion, it is not clear that even the largest current computers make this possible, especially if the thicker reattaching layer demands values of  $L_z/L$  larger than 0.1.

A relatively easy study of some interest will be to design boundary conditions that produce a flow with the same pressure distribution, but on a straight wall. This will isolate the pressure-gradient effects from the wall-curvature effects. This work has not started.

A general conclusion is that DNS of smooth-body separation on non-trivial geometries is just now becoming possible in the 2020's, following the successful studies over straight walls with Reynolds-number

variations due to [Coleman et al. \(2018\)](#) and [Abe \(2017\)](#) in the 2010's. [Spalart et al. \(2017\)](#) have conducted an embedded DNS of the Bachalo-Johnson flow, but the domain width was also insufficient after separation. The Reynolds numbers reachable by DNS remain barely sufficient to assess theories and RANS models. Exascale computing resources, if the DNS codes adapt well to them, will be very valuable.

#### Declaration of Competing Interest

The authors declare that they have no known competing financial interests or personal relationships that could have appeared to influence the work reported in this paper.

#### Acknowledgements

The simulations were conducted with the use of the cluster Tornado of the Computer Center “Polytechnichesky”. The research of the Russian

authors was funded by the Ministry of Science and Higher Education of the Russian Federation as part of World-class Research Center program: Advanced Digital Technologies (contract No. 075-15-2020-934 of 17.11.2020).

## References

- Abe, H., 2017. Reynolds-number dependence of wall-pressure fluctuations in a pressure-induced turbulent separation bubble. *J. Fluid Mech.* 833, 563–598. <https://doi.org/10.1017/jfm.2017.694>.
- Bachalo, W.D., Johnson, D.A., 1986. Transonic, turbulent boundary-layer separation generated on an axisymmetric flow model. *AIAA J.* 24 (3), 437–443. <https://doi.org/10.2514/3.9286>.
- Balin, R., Jansen, K.E., Spalart, P.R., 2020. Wall-Modeled LES of flow over a Gaussian bump with strong pressure gradients and separation. *AIAA Paper 2020-3012*. <https://doi.org/10.2514/6.2020-3012>.
- Bentaleb, Y., Lardeau, S., Leschziner, M.A., 2012. Large-eddy simulation of turbulent boundary layer separation from a rounded step. *Journal of Turbulence*, 13 (4), <https://doi.org/10.1080/14685248.2011.637923>.
- Bradshaw, P., 1973. The effects of streamline curvature on turbulent flow. AGARDograph No. 169.
- Coleman, G.N., Rumsey, C.L., Spalart, P.R., 2018. Numerical study of turbulent separation bubbles with varying pressure gradient and Reynolds number. *J. Fluid Mech.* 847, 28–70. <https://doi.org/10.1017/jfm.2018.257>.
- Disotell, K.J., Rumsey, C.L., 2017. Design of an axisymmetric afterbody test case for CFD validation. *AIAA Paper 2017-3792*. <https://doi.org/10.2514/6.2017-3792>.
- Eisfeld, B., Rumsey, C., Togiti, V., 2016a. Verification and validation of a second-moment-closure model. *AIAA Journal* 54 (5), 1524–1541. <https://doi.org/10.2514/1.J054718>.
- Eisfeld, B., Rumsey, C., Togiti, V., 2016b. Erratum: Verification and validation of a second-moment-closure model. *AIAA J.* 54 (9), 2927–2928. <https://doi.org/10.2514/1.J055336>.
- Greenblatt, D., Paschal, K.B., Yao, C.-S., Harris, J., Schaeffler, N.W., Washburn, A.E., 2006. Experimental investigation of separation control Part 1: Baseline and steady suction. *AIAA J.* 44 (12), 2820–2830. <https://doi.org/10.2514/1.13817>.
- Knopp, T., Buchmann, N.A., Schanz, D., Eisfeld, B., Cierpka, C., Hain, R., Schröder, A., Kähler, C.J., 2015. Investigation of scaling laws in a turbulent boundary layer flow with adverse pressure gradient using PIV. *J. Turbul.* 16 (3), 250–272. <https://doi.org/10.1080/14685248.2014.943906>.
- Lowe, T., Beardsley, C., Borgoltz, A., Devenport, W.J., Duetsch-Patel, J.E., Fritsch, D.J., Gargiulo, A., Roy, C.J., Máté Szoke, M., Vishwanathan, V., 2020. Status of the NASA/Virginia Tech Benchmark experiments for CFD validation. *AIAA Paper 2020-1584*. <https://doi.org/10.2514/6.2020-1584>.
- Lynch, K.P., Lance, B.W., Lee, G.S., Naughton, J.W., Miller, N.E., Barone, M.F., Beresh, S.J., Spillers, R.W., Soehnel, M.M., 2020. A CFD validation challenge for transonic, shock-induced separated flow: Experimental characterization. *AIAA paper 2020-1309*. <https://doi.org/10.2514/6.2020-1309>.
- Menter, F.R., 1994. Two-equation eddy-viscosity turbulence models for engineering applications. *AIAA J.* 32 (8), 1598–1605. <https://doi.org/10.2514/3.12149>.
- NASA Langley Research Center, Turbulence Modeling Resource, VERIF/2DB: 2D Bump-in-channel Verification Case - Intro Page: <https://turbmodels.larc.nasa.gov/bump.html>, last visited 19.05.2021.
- Rogers, S.E., Kwak, D., 1988. An upwind differencing scheme for the time-accurate incompressible Navier-Stokes equations. *AIAA Paper 1988-2583*. <https://doi.org/10.2514/6.1988-2583>.
- Rumsey, C.L., 2018. The NASA juncture flow test as a model for effective CFD/experimental collaboration. *AIAA Paper 2018-3319*. <https://doi.org/10.2514/6.2018-3319>.
- Shur, M., Strelets, M., Travin, A., 2004. High-order implicit multi-block Navier-Stokes code: ten-year experience of application to RANS/DES/LES/DNS of turbulent flows. In: 7th Symp. On Overset Composite Grids and Solution Technol. Huntington Beach, CA, [https://cfd.spbstu.ru/agarbaruk/doc/NTS\\_code.pdf](https://cfd.spbstu.ru/agarbaruk/doc/NTS_code.pdf), last visited 19.05.2021.
- Shur, M.L., Spalart, P.R., Strelets, M.K., Travin, A.K., 2014. Synthetic turbulence generators for RANS-LES interfaces in zonal simulations of aerodynamic and aeroacoustic problems. *Flow Turbul. Combust.* 93 (1), 63–92. <https://doi.org/10.1007/s10494-014-9534-8>.
- Simmons, D., Thomas, F.O., Corke, T.C., 2019. Smooth body flow separation experiments and their surface flow topology characterization. *AIAA Paper 2019-3085*. <https://doi.org/10.2514/6.2019-3085>.
- Slotnick, J.P., 2019. Integrated CFD validation experiments for prediction of turbulent separated flows for subsonic transport aircraft. *STO-MP-AVT 6-1, 6–13*.
- Spalart, P.R., Allmaras, S.R., 1992. A one-equation turbulence model for aerodynamic flows. *AIAA Paper 1992-2439*. <https://doi.org/10.2514/6.1992-439>.
- Spalart, P.R., Watmuff, J.H., 1993. Experimental and numerical study of a turbulent boundary layer with pressure gradients. *J. Fluid Mech.* 249, 337–371. <https://doi.org/10.1017/S002211209300120X>.
- Spalart, P.R., Shur, M.L., 1997. On the sensitization of turbulence models to rotation and curvature. *Aerosp. Sci. Technol.* 1 (5), 297–302. [https://doi.org/10.1016/S1270-9638\(97\)90051-1](https://doi.org/10.1016/S1270-9638(97)90051-1).
- Spalart, P.R., Strelets, M., Travin, A., 2006. Direct numerical simulation of large-eddy-break-up devices in a boundary layer. *Int. J. Heat Fluid Flow* 27 (5), 902–910. <https://doi.org/10.1016/j.ijheatfluidflow.2006.03.014>.
- Spalart, P.R., Shur, M.L., Strelets, M.K., Travin, A.K., 2015. Direct Simulation and RANS Modelling of a Vortex Generator Flow. *Flow Turbul. Combust.* 95 (2-3), 335–350. <https://doi.org/10.1007/s10494-015-9610-8>.
- Spalart, P.R., Belyaev, K.V., Garbaruk, A.V., Shur, M.L., Strelets, M.K., Travin, A.K., 2017. Large-eddy and direct numerical simulations of the Bachalo-Johnson flow with shock-induced separation. *Flow Turbul. Combust.* 99 (3), 865–885. <https://doi.org/10.1007/s10494-017-9832-z>.
- Spalart, P.R., Garbaruk, A.V., 2020. Correction to the Spalart-Allmaras turbulence model, providing more accurate skin friction. *AIAA J.* 58 (5), 1903–1905. <https://doi.org/10.1007/s10494-014-9534-8>.
- Uzun, A., Malik, M.R., 2020. Simulation of a turbulent flow subjected to favorable and adverse pressure gradients. *AIAA Paper 2020-3061*. <https://doi.org/10.2514/6.2020-3061>.
- Uzun, A., Malik, M.R., 2018. Large-Eddy Simulation of flow over a wall-mounted hump with separation and reattachment. *AIAA J.* 56 (2), 715–730. <https://doi.org/10.2514/1.J056397>.
- Williams, O., Samuell, M., Sarwas, E.S., Robbins, M., Ferrante, A., 2020. Experimental study of a CFD Validation Test Case for Turbulent Separated Flows. *AIAA Paper*, 2020-0092, <https://doi.org/102514/6.2020-0092>.